Available online at www.sciencedirect.com
ScienceDirect
Biochimica et Biophysica Acta 1758 (2006) 814–829
BIOCHIMICA ET BIOPHYSICA ACTA
BBA
www.elsevier.com/locate/bbamem

Review

Spatial resolution in infrared microspectroscopic imaging of tissues

Peter Lasch *, Dieter Naumann

P25 "Biomedical Spectroscopy", 13353 Berlin, Nordufer 20, Germany

Received 12 March 2006; received in revised form 5 June 2006; accepted 5 June 2006
Available online 9 June 2006

Abstract

Spatial resolution is one of the most critical measurement parameters in infrared microspectroscopy. Due to the distinct levels of morphologic heterogeneity in cells and tissues the spatial resolution in a given IR imaging setup strongly affects the character of the infrared spectral patterns obtained from the biomedical samples. This is particularly important when spectral data bases of reference microspectra from defined tissue structures are collected. In this paper we have also pointed out that the concept of spatial resolution in IR imaging is inseparable from the contrast. Based on infrared microspectroscopic transmittance data acquired from an USAF 1951 resolution target we have demonstrated how the spatial resolution can be determined experimentally and some numbers for the spatial resolution of popular IR imaging systems are provided. Finally, we have presented a new computational procedure which is suitable to improve the spatial resolution in IR imaging. A theoretical model of 3D-Fourier self-deconvolution (FSD) is given and advantages or pitfalls of this method are discussed. Based on synchrotron IR microspectroscopic data we have furthermore demonstrated that the technique of 3D-FSD can be successfully applied to increase the spatial resolution in a real IR imaging setup.

Keywords: Biomedical infrared spectroscopy; Spatial resolution; IR microspectroscopy of Tissue

Contents

1. Introduction . . . 815
2. Spatial resolution–definition and determination . . . 815
   2.1. Definitions of lateral spatial resolution . . . 815
   2.2. The contrast of a test pattern can be used to quantify spatial resolution . . . 817
   2.3. Examples for the determination of the spatial resolution from experimental data . . . 818
      2.3.1. Experimental . . . 820
3. Spatial resolution in FT-IR imaging of tissues in practice . . . 820
   3.1. Detection of prion protein deposits in neurons of scrapie-infected hamsters . . . 820
   3.2. Spatial resolution in IR imaging of the colon mucosa . . . 821
4. Increasing spatial resolution by 3D-Fourier self-deconvolution (FSD) . . . 824
   4.1. Theory of FSD and 3D-FSD . . . 825
   4.2. Practical limitations of 3D-FSD . . . 826
   4.3. Example of resolution enhancement by 3D-Fourier self-deconvolution . . . 827
5. Conclusions . . . 827
Acknowledgements . . . 828
References . . . 828

Abbreviations: FSD, Fourier self-deconvolution; FT-IR, Fourier transform infrared; IR, infrared; MCT, mercury cadmium telluride; MTF, modulation transfer function; PSF, point spread function; SNR, signal-to-noise ratio

* Corresponding author. Tel.: +49 30 45472405; fax: +49 30 45472606.
E-mail address: LaschP@rki.de (P. Lasch).

0005-2736/$ - see front matter © 2006 Elsevier B.V. All rights reserved.
doi:10.1016/j.bbamem.2006.06.008

1. Introduction

The past decade has witnessed a tremendous increase of research activity in the field of biomedical Fourier transform infrared (FT-IR) spectroscopy [1–3]. Particularly, infrared microspectroscopy, the combination of IR spectroscopy and microscopy has been increasingly applied to study human tissues and–more importantly–tissue pathologies [4,5]. Since the mid-1990's, new technical developments such as multichannel detectors or synchrotron IR microspectroscopy permit high-quality infrared microspectroscopic imaging of biomedical samples [3,6–10]. The IR imaging methodology provides spatially resolved structural and compositional information on the histological specimens and, in combination with computer based multivariate image reassembling techniques, opens wide perspectives for routine use in the clinical environment.

IR spectroscopy is a rapid photonic technique that can be used to generate image contrast on the basis of the tissue's intrinsic biochemical composition. Hence, no staining or labeling procedures are required. In this way, the biochemical integrity of the tissues is not compromised by stains or dyes. Furthermore, the technique of FT-IR microspectroscopic imaging produces false color maps that are derived either directly from distinct spectral parameters (functional group mapping) [1,9], or alternatively, from similarity measures obtained by pattern recognition techniques from complete spectra [11]. It is a strength of the technique that these images are directly comparable to outcomes of standard histological staining protocols and can be interpreted also by non-spectroscopists.

In IR imaging, as for any type of optical microscopy, the parameter of lateral spatial resolution is one of the most critical factors defining image fidelity. The spatial resolution – in the present work we purposely ignore the axial component and refer only to the lateral resolution – strongly defines the type of objects to be studied. Naturally, biological samples such as tissues are composed of diverse structural units which exhibit heterogeneity at several microscopic levels: heterogeneity can be found at low power magnifications between distinct types of tissues (i), at higher resolutions between individual cells (ii), or at the submicron scale between subcellular structures (iii). Hence, the magnification factor (or more exactly, the spatial resolution) of an optical system determines which types of objects are examined. This obvious fact is well known in clinical histopathology as tissue specimens are routinely investigated at various magnifications. To give an example, histopathological examination usually starts at a low magnification with the examination of the gross morphologic changes and ends up with an evaluation of the morphology of subcellular structures, such as nuclear polarity of tumor cells.

One of the shortcomings of the infrared imaging method is the inherently low lateral spatial resolution. In any type of (far field) optical microscopy the spatial resolution is restricted by the so-called diffraction limit which is in the order of the wavelength λ of the imaging light:

$$\Delta x \geq 0.61 \cdot \frac{\lambda}{n \sin\theta} \quad (1)$$

In Eq. (1) Δx is the distance separating two objects and n is the refractive index of the medium between the objective and the specimen. Furthermore, θ denotes the acceptance angle of the objective. The term $n\ sin\theta$ is commonly known as the numerical aperture (N.A.) of the objective. Eq. (1) is derived from Rayleigh's criterion which states that two points can be resolved as long as the center of one Airy disk coincides with the first minimum (zero crossing) of the second Airy pattern (for details see e.g. refs. [12–14]).

It is important to note that Eq. (1) describes only the principal limitations of lateral spatial resolution in far-field optical microscopy. In practice, the optical design (e.g. mirrors, objectives, apertures, detector geometry) and factors that may have an effect on the spectral SNR (source brightness, detector response, sample definition, etc.) further reduce the effective resolution of the microspectroscopic technique [15].

One obvious conclusion from Eq. (1) is that due to the long wavelength of mid-infrared light (λ=2.5–10 μm) the lateral resolution of IR based microscopes will be always inferior compared to microscopes using light in the visible range. This drawback is, however, compensated by the much higher amount of information available in the spectral domain. While microscopy in the visual range usually provides only three (RGB) or four (CMYK) 8-bit color values per image pixel, infrared microspectroscopy produces per pixel a complete spectrum of up to several thousands IR intensity values. This enormous amount of qualitative and quantitative information can be directly related to the samples' biochemical and structural composition and can be used in various fields of research.

In this paper we will first demonstrate how the lateral spatial resolution can be determined experimentally. We will also give two practical examples demonstrating how the detectability of uni- and multivariate disease markers depends on the spatial resolution in a given IR microspectroscopic setup. Finally, a computational approach for increasing the spatial resolution in IR imaging is presented and discussed.

2. Spatial resolution–definition and determination

2.1. Definitions of lateral spatial resolution

Various research communities have a different understanding of what lateral spatial resolution is. An often-cited definition is the −3 dB width of the impulse response within the image from an infinitesimally small feature [13]. In computer techniques spatial resolution is used as a measure of the accuracy or detail of a graphic display, expressed as dots per inch (dpi), pixels per line, or lines per millimeter (lp/mm). Another often cited definition for lateral spatial resolution was derived from the above-mentioned Rayleigh criterion: two points can be separated when the central maximum of the first

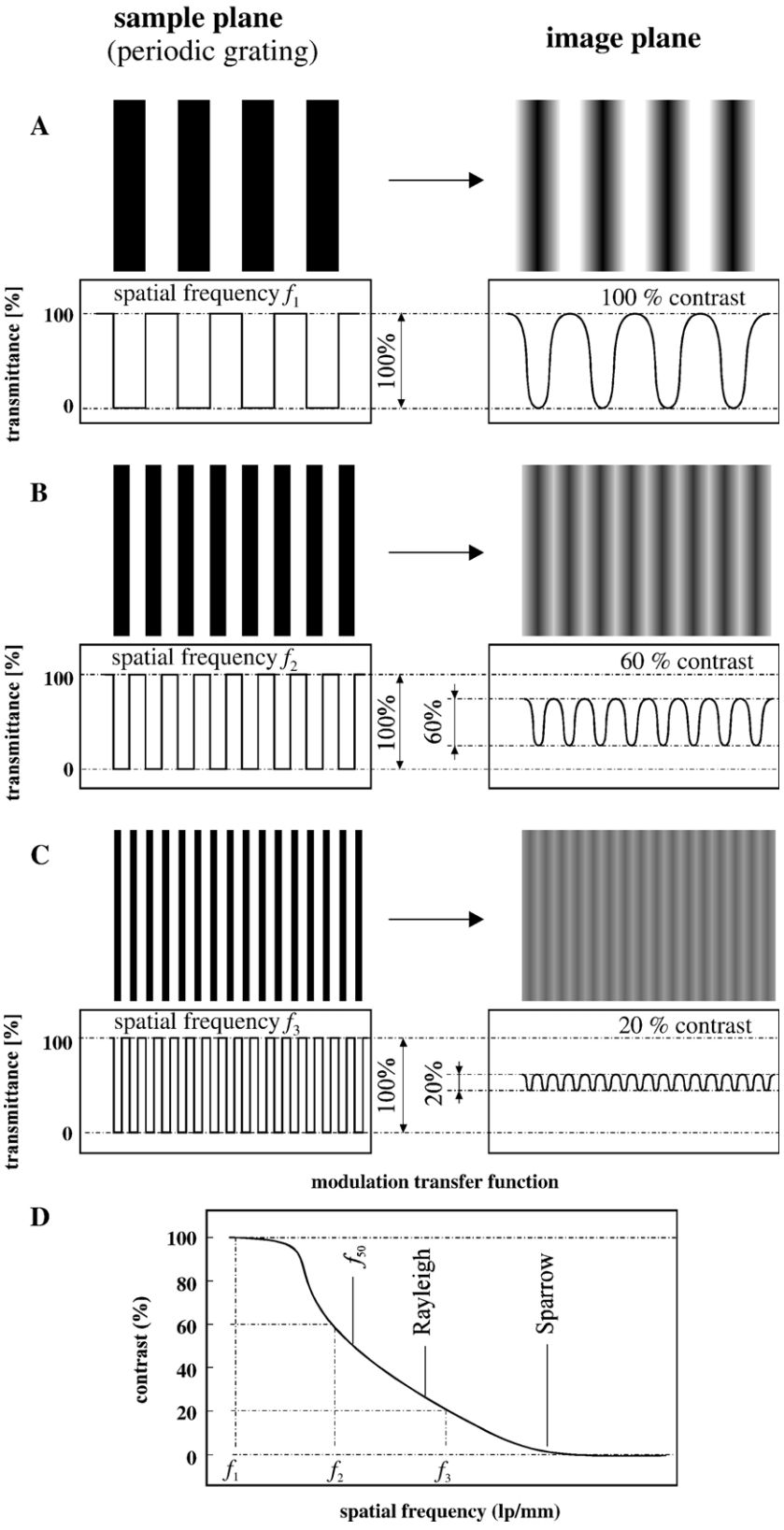

Fig. 1. The modulation transfer function (MTF). Illustration of interdependence between image contrast and the spatial frequency. A periodic line grating pattern composed of black and white lines of equal width with a spatial frequency *f* is transferred by an optical system to the image plane. The resulting image contrast of the bar pattern is obtained and plotted as a function of the spatial frequency (see text for details).

Airy disk is just one radius away of the other one [e.g. 12,14]. Rayleigh's criterion of separation corresponds under ideal conditions to a distinct contrast value, namely of 26.4%. There are certainly other contrast values conceivable which could be principally used to define the parameter of lateral spatial resolution. To give an example, the so-called Sparrow criterion defines resolution of an optical system as the distance where the saddle point of the sum of the two Airy disks first develops i.e., the distance at which the slope at the peak of the summed profile equals zero (cut-off distance). Another approach that uses image contrast for determining the resolving power is based on the area under the contrast vs. spatial frequency curves. This is particularly useful in cases where optical aberrations affect the resolving power of the microscopes. Thus, image contrast and resolution are two related parameters and any contrast value could be principally used for the definition of the spatial resolution.

The contrast between two neighboring structures in the image plane is defined as follows:

$$C(\lambda) = \frac{I_1(\lambda) - I_2(\lambda)}{I_1(\lambda) + I_2(\lambda)} \quad (2)$$

Where I_1 is the light intensity of the brighter and I_2 the intensity of the darker object. If numerator and denominator of Eq. (2) are both divided by $I_o(\lambda)$, the intensity of the incident light, Eq. (2) can be also written as

$$C(\lambda) = \frac{T_1(\lambda) - T_2(\lambda)}{T_1(\lambda) + T_2(\lambda)} \quad (3)$$

The transmittance $T(\lambda)$ can be directly obtained from the IR microspectra.

2.2. The contrast of a test pattern can be used to quantify spatial resolution

In the present work we have examined the contrast pattern infrared microscopes produce in the image plane as a response to a periodic grating pattern in the sample plane (see Fig. 1). These periodic test bar patterns consist usually of a number of bar groups that contain alternating black and transparent lines of equal width. The number of line pairs per millimeter (lp/mm) is commonly known as the spatial frequency. The examination of periodic gratings by diffraction limited optical systems such as modern IR microspectrometers reveals sinusoidal intensity profiles in the image plane which may vary between full (i.e. 100%) and no (0%) contrast. The relation between the contrast and spatial frequency is commonly referred to as the modulation transfer function (MTF).

The calculated example of Fig. 1 illustrates how the contrast function in the image plane changes as the spatial frequency f is varied. At a low spatial frequency f_1 the output intensity of the optical microscope varies between 0 and 100%, i.e. a contrast of 100% is achieved (cf. Fig. 1A). At higher spatial frequencies the sinusoidal throughput response is altered and varies between 20 and 80% (f_2) or 40 and 60% (f_3), respectively. As

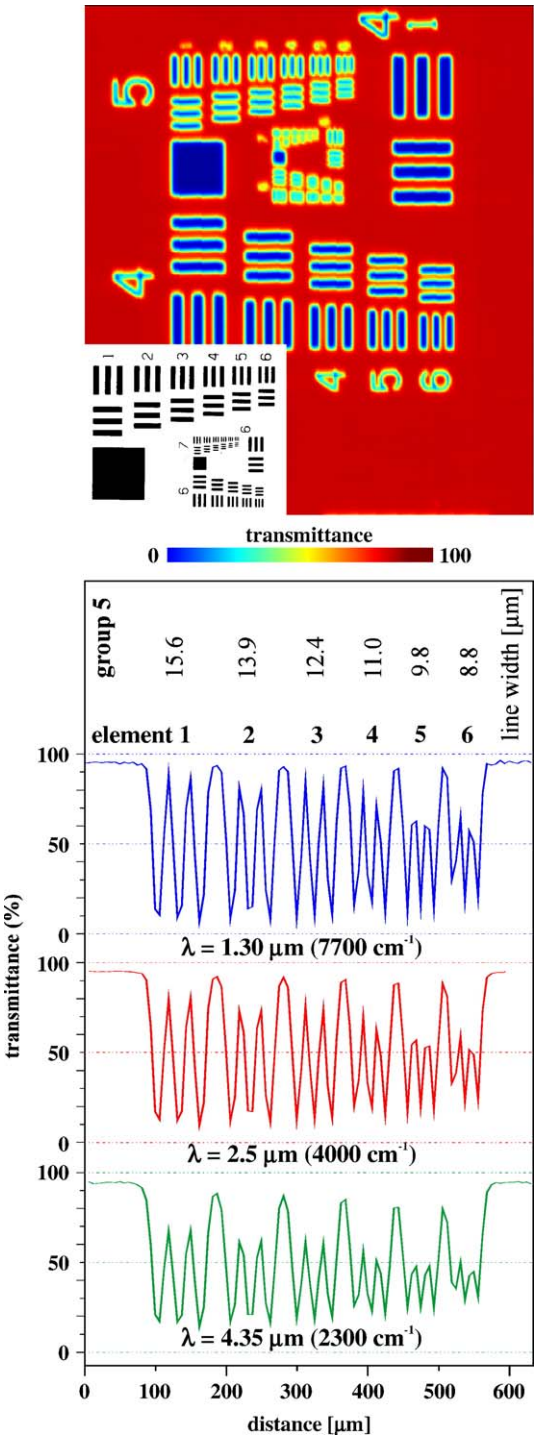

Fig. 2. Spatial resolution of the PerkinElmer Spectrum Spotlight 300 system. Transmission type FT-IR measurements of an USAF 1951 standard resolution target in the 4:1 imaging mode. Upper panel: IR image reassembled from transmission spectra at 2.5 µm (4000 cm^{-1}). Area size: 1300×1144 µm (209×184 spectra). Lower left corner: brightfield multiwavelength image of the resolution target in the visible range (380–740 nm). Lower panel: transmission profiles of the group 5 elements at various infrared wavelengths: 1.43 µm (blue curve, 7700 cm^{-1}), 2.5 µm (red curve, 4000 cm^{-1}), and 4.35 µm (green curve, 2300 cm^{-1}). At 2.5 µm wavelength the Rayleigh criterion (26.4% contrast) was reached by the use of the target element 6 of group 5. This corresponds to a spatial resolution of about 8.8 µm (see text for details).

a consequence the image contrast is reduced to 60% (Fig. 1B) or 20% (Fig. 1C). Fig. 1D shows exemplary the modulation transfer function that was derived from the calculated examples of Fig. 1A–C.

In IR microspectroscopy one can utilize the transmittance instead the intensity for obtaining the contrast (cf. Eqs. (2) and (3)). Furthermore, if periodic test bar patterns of equal bar width are analyzed, the sum of maximum and minimum transmittance values $T_1(\lambda)$ and $T_2(\lambda)$, respectively, should be equal 100. Consequently, Eq. (3) can be simplified in the following way:

$$C(\lambda) = \frac{T_1(\lambda) - T_2(\lambda)}{100} * 100\% \quad (4)$$

In practice, the MTF of a microscope or scanner is frequently used to determine the spatial resolution. In the following we will refer to the spatial frequency at 26.4% image contrast (Rayleigh criterion) as the pertinent parameter of spatial resolution.

Direct measurements of the MTF can be carried out by utilizing specific pattern targets such as the USAF 1951 3-bar resolving power test target. This target contains numbered bar groups each consisting of six test target elements. The change of the spatial frequency of these test target elements is in a geometric progression based on the sixth root of 2. Other resolution targets like the microscopy resolution test charts NBS 1010A are based on very similar principles.

Experimental modulation transfer functions are obtained by determining the specific contrast produced by bar group patterns of various spatial frequencies (see Eq. (4)).

2.3. Examples for the determination of the spatial resolution from experimental data

In order to obtain the modulation transfer function (MTF) for modern FT-IR microspectrometers, the USAF 1951 resolution target was characterized by a PerkinElmer Spectrum Spotlight, a Bruker Hyperion 3000 and a Bruker A590 FT-IR imaging system. The results of these microspectroscopic measurements are given in Fig. 2 (Spectrum Spotlight) and Fig. 3 (Hyperion, 36× Cassegrain objective). Both figures display in their upper panels color scaled transmittance maps at 4000 cm^{-1} (2.5 μm) and in the lower panels examples of line scans through selected bar groups (group 5 in Fig. 2 and group 7 in Fig. 3).

The transmittance profiles in Figs. 2 and 3 exhibit a clear dependence of the contrast on the wavelength: the shorter the wavelength the higher the contrast. This finding is what Abbe's theory of diffraction limited optical systems predicts (see Eq. (1)).

The MTF for the Spectrum Spotlight as well as for the two Bruker microspectrometers were then derived from line scan profiles that could be extracted directly from the IR transmittance imaging data (Fig. 4). Line scans were obtained from bar groups 4–7. As shown by Fig. 4, the experimentally obtained MTF curves fit reasonably well with the theory, i.e. the contrast decreases with increasing spatial frequencies of the test bars. Furthermore, the contrast at shorter wavelengths is with one exception larger than the respective contrast at longer wavelengths.

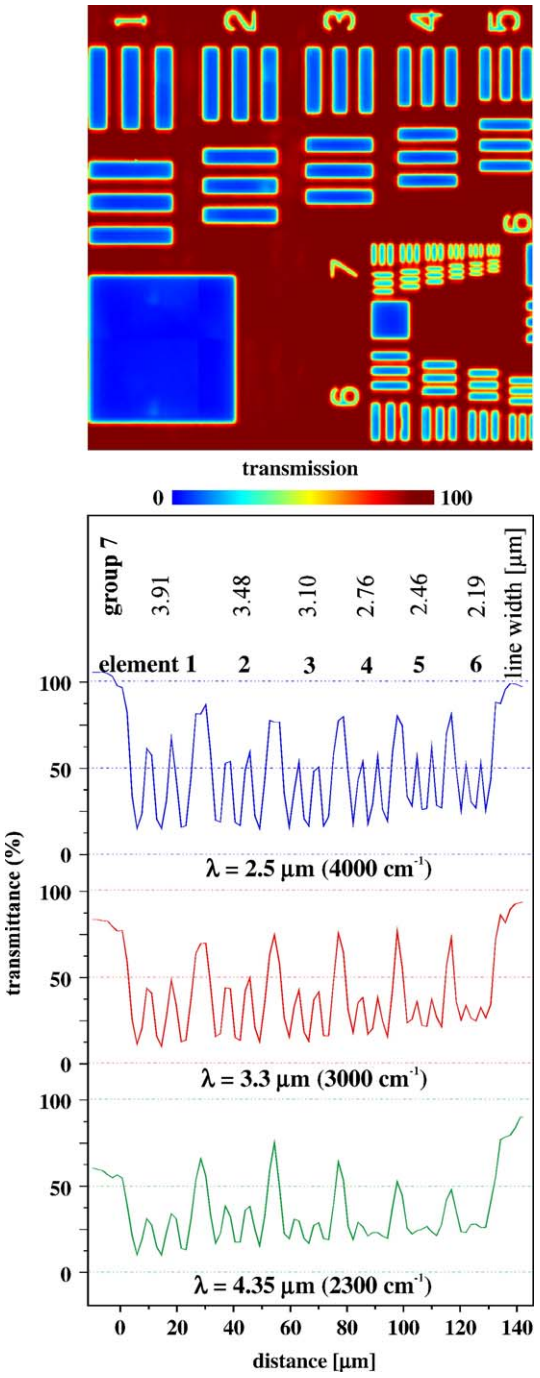

Fig. 3. Spatial resolution of the Bruker Hyperion 3000 system. Transmission type FT-IR measurements of an USAF 1951 standard resolution target using a 36×Cassegrain objective. Upper panel: IR image reassembled from transmission spectra at 2.5 μm (4000 cm^{-1}). Area size: 444×444 μm (256×256 spectra). Lower panel: transmission profile of group 7 elements for various infrared wavelengths: 2.5 μm (blue curve, 4000 cm^{-1}), 3.33 μm (red curve, 3000 cm^{-1}), and 4.35 μm (green curve, 2200 cm^{-1}). At 2.5 μm wavelength the Rayleigh criterion (26.4% contrast) was reached at the target element 5 of group 7. This corresponds to a spatial resolution of ca. 2.4 μm (see text for details).

To obtain precise values for the lateral spatial resolution the experimentally MTF curves were fitted and spatial frequencies at contrast values of 50%, 26.4% (Rayleigh criterion), and 0% (Sparrow criterion) were determined. The results of these

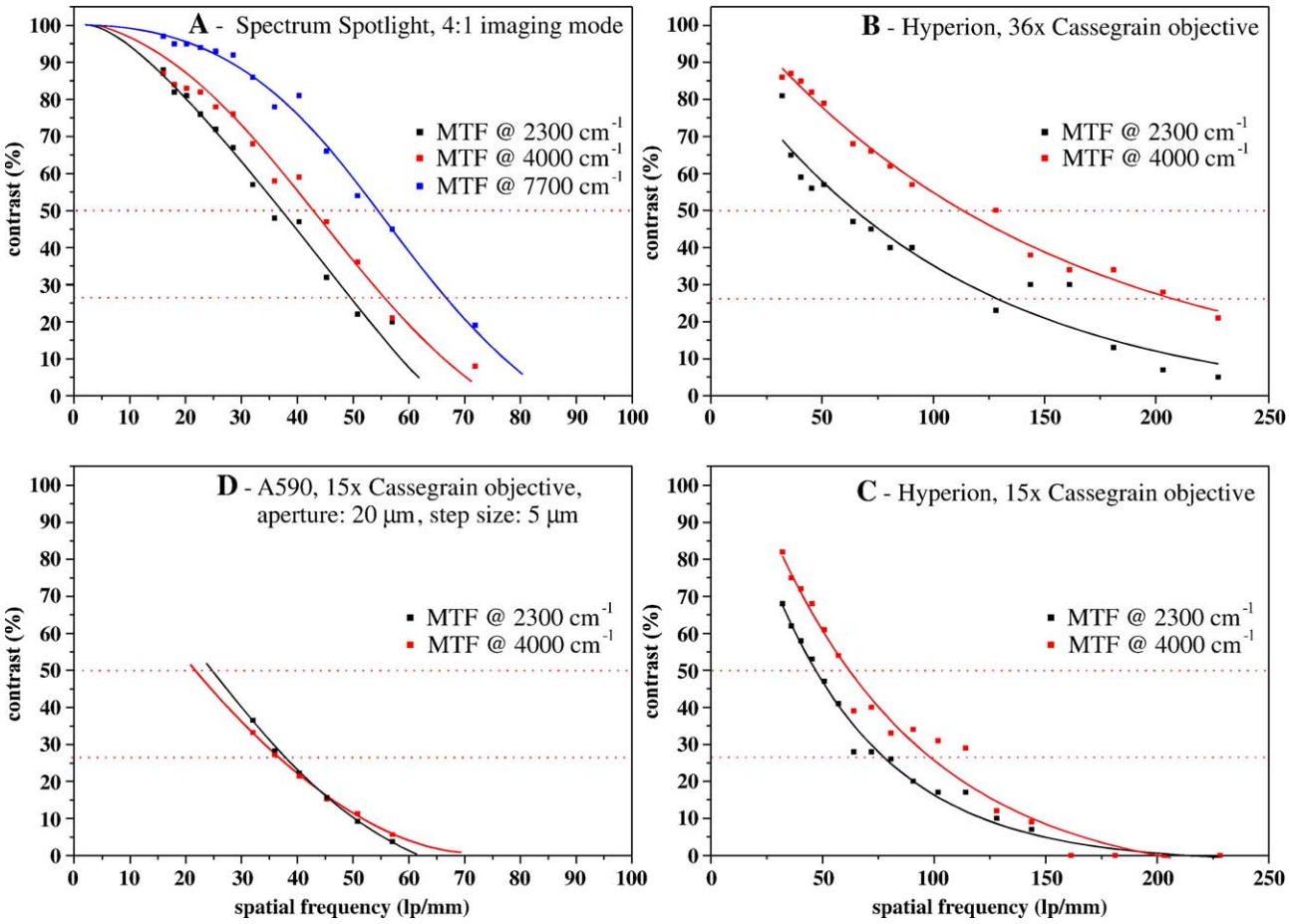

Fig. 4. Modulation transfer functions (MTF) experimentally obtained by analysis of transmittance spectra of an USAF 1951 standard resolution target. Experimental MTFs are obtained by determining the specific contrast produced by bar group patterns of various spatial frequencies (see Eq. (4)). Panel A: MTF of the PerkinElmer Spectrum Spotlight microspectrometer (4:1 imaging mode) Panel B: MTF of the Bruker Hyperion 3000 imaging system (36× objective) Panel C: MTF of the Bruker Hyperion 3000 imaging system (15× objective) Panel D: MTF of the Bruker A590 microspectrometer (see text for details).

computations are given in Table 1. In this table, the spatial resolution is given in units of the spatial frequency and also in distance units (µm). Conversion from one unit into another was achieved according to $s=1000/(2*f)$.

The evaluation of the spatial resolution values summarized in Table 1 reveals that modern IR imaging microspectrometers are diffraction limited optical systems. In addition, the spatial resolution of the Hyperion microscope of 2.4 µm at $\lambda=2.5$ µm (Rayleigh-criterion, see Table 1) seems to be even better than the theoretical limit. According to Eq. (1), the spatial resolution cannot exceed 3.05 µm ($N.A._{36\times}=0.5$). We believe that an interpretation of this unforeseen experimental finding should account for the precise optical configuration of the Hyperion microspectrometer which is unfortunately not known to us. It is well recognized, for example, that Eq. (1) does not account for the behavior of the condenser present in the Hyperion microscope. This and other factors are also elements that may affect the effective spatial resolution.

Table 1
The spatial resolution of IR imaging systems: A: PerkinElmer Spectrum Spotlight system (16×1 staggered detector array, 4:1 imaging mode), B and C

	Units	A: Spectrum Spotlight 4:1 imaging mode			B: Hyperion Cassegrain 15×		C: Hyperion Cassegrain 36×		D: A590, circ. apt ∅ 20 µm step size: 5 µm	
		2300 cm^1	4000 cm^1	7700 cm^1	2300 cm^1	4000 cm^1	2300 cm^1	4000 cm^1	2300 cm^1	4000 cm^1
Sparrow f_0, cut-off	[lp/mm]	~65	~74	~85	~200	~200	~250	~350	~63	~64
	[µm]	7.7	6.8	5.9	2.5	2.5	2.0	1.42	7.9	7.8
Rayleigh $f_{26.4}$	[lp/mm]	51.0	56.6	66.5	77.0	98.5	128	206	37.2	36.2
	[µm]	10.4	8.8	7.5	6.5	5.1	3.9	2.4	13.4	13.8
f_{50}	[lp/mm]	36.9	43.9	55.0	47.0	61.9	65.5	113	26.3	24.2
	[µm]	13.5	11.4	9.1	10.6	8.1	7.6	4.4	19.0	20.7

Bruker Hyperion FT-IR 64×64 FPA imaging system equipped with an 15×(N.A.= 0.4), or, 36×Cassegrain objective (N.A.= 0.5), D: Bruker A590 IR microscope. An USAF 1951 resolution target was used as a test pattern to obtain the modulation transfer functions (MTF) for the FT-IR microspectroscopic imaging systems.

For the Bruker A590 microscope we have noted that at low spatial frequencies (<45 lp/mm) the contrast at 4000 cm^{-1} is apparently somewhat smaller than the contrast at 2300 cm^{-1}. This unexpected observation needs some clarification (Fig. 4D).

In the previous chapters we have implicitly assumed that chromatic aberrations are sufficiently small in the given experimental setup. This certainly holds true for modern IR microspectrometers. However, the resolution target, or an IR window on which the cells or tissues are mounted consists usually of dispersive materials that give rise to a focus shift between various wavelengths. Unfortunately, these chromatic aberrations of the window material cannot be readily corrected (for details refer to [16]). As a consequence, each of the wavelengths will have their own focus position. Naturally, a sample which is out of focus will give a poorer spatial resolution compared to a sample within the proper focus position. Hence, the main conclusion that can be drawn is that the spatial resolution obtained in transmission type measurements with polychromatic light will be precise only for the wavelength in focus position. We believe that the low contrast at 2.5 μm in Fig. 4D is biased by these chromatic aberrations.

A detailed analysis of the MTF curves point to another problem of the IR microspectroscopic imaging method. Some of these curves display stair-step artifacts, particularly at higher spatial frequencies (see Fig. 4B/C). We have interpreted these artifacts as a result of undersampling. According to Shannon's sampling theorem a signal can be perfectly reconstructed if the sampling frequency is at least twice as high as the maximum signal frequency [17]. For two-dimensional signals, such as images, this means that discrete sampling by a CCD camera or a MCT focal plane array detector should utilize a sampling interval that is not larger than one-half the size of the smallest resolvable sample feature. This is equivalent to acquiring images at twice the highest spatial frequencies contained in the samples (Nyquist criterion, [18]). For instance, if in a given sample the spatial frequency of certain elements is 50 lp/mm, the IR imaging device must sample at intervals that correspond in the specimen plane to 100 lp/mm or more. Otherwise, the sample is undersampled and frequencies that are above this limit will be aliased and appear in the resulting image as lower frequencies. Oversampling, in turn, will not add more details to the resulting images.

It is interesting to note that the MTF of definitely oversampled maps (panel D) are smooth and do not show the stair-step patterns of panels B/C. Thus, undersampling may be the reason for the artifacts in the MTF curves of the FPA imaging devices.

2.3.1. Experimental

The resolution target used was a USAF 1951 standard resolution target obtained from Edmund Optics (Barrington, NJ, USA). The test target substrate was soda lime glass of a thickness of 1.5 mm at which a chromium test pattern was vacuum-deposited. IR target measurements were carried out in transmission mode. Note that the optical properties of the target substrate (glass) hindered IR transmission measurements below 2200 cm^{-1}.

Mid-infrared images of the resolution target were obtained by the Spectrum Spotlight system (PerkinElmer Instruments, Shelton, CT, USA), the Hyperion 3000 IR imaging system and an A590 microscope (both from Bruker Optik GmbH, Ettlingen, Germany). The PerkinElmer microspectrometer system consisted of a Spectrum Spotlight One FT-IR spectrometer coupled to a Spectrum Spotlight 300 infrared microscope. The microscope was equipped with a staggered 16×1 element (400×15 μm^2) HgCdTe (MCT) array detector and connected to a computer controlled *xy*-stage. Microscope optics permits 1:1 or 4:1 imaging, resulting in sample areas of 25×25 or 6.25×6.25 μm^2 projected onto each detector element. For IR imaging of the resolution target, the 4:1 imaging mode was used. Spectra were recorded from 2200 to 8000 cm^{-1} at a nominal spectral resolution of 8 cm^{-1}.

The Hyperion 3000 FT-IR imaging system from Bruker comprised an IFS-66 infrared spectrometer coupled to the Hyperion IR microscope equipped with a 64×64 MCT focal plane array (FPA) detector. A software controlled *xy*-stage permitted precise stitching of the FPA images. Resolution target measurements were carried out in transmission mode, using a 15× and 36× Cassegrain objective. Spectra were recorded from 2200 to 4000 cm^{-1} at a nominal spectral resolution of 16 cm^{-1}.

Resolution target measurements were additionally carried out by utilizing a Bruker A590 IR microscope connected to an IFS 28B spectrometer. The microscope was equipped with a small-sized 100×100 μm^2 single element MCT detector and a motor-driven *xy*-stage. A circular aperture of 20 μm diameter restricted the sample area illuminated by the IR radiation and a step size of the *xy*-stage of 5 μm was chosen. Transmission type IR spectra were recorded from 2200 to 8000 cm^{-1} at a spectral resolution of 16 cm^{-1}.

3. Spatial resolution in FT-IR imaging of tissues in practice

The following chapter addresses practical aspects of spatial resolution in IR microspectroscopy of tissues. We will give two examples that illustrate how spatial resolution and the detectability of uni- and multivariate disease markers in IR microspectra of tissues are interrelated.

3.1. Detection of prion protein deposits in neurons of scrapie-infected hamsters

The family of transmissible spongiform encephalopathies (TSE) is characterized by the structural change of a normal cellular protein, the prion protein (PrP^C) into its misfolded and aggregated isoform PrP-scrapie, or PrP^{Sc}. The pathology of this fatal neurological disorder includes the accumulation of PrP^{Sc} within neurons, which is followed by neuronal loss, and the formation of vacuoles or microcavities within the nervous tissue. Both of the isoforms, PrP^C and PrP^{Sc}, exhibit characteristic mid-infrared spectral signatures permitting its differentiation by infrared spectroscopy. In an attempt to identify PrP^{Sc} aggregates and the scrapie associated fibrils *in situ*, Kneipp et al., utilized a synchrotron IR source to study cryosections of dorsal root ganglia from scrapie-infected Syrian hamsters [19,20]. In this series of microspectroscopic investigations an aperture size of 10×10 μm^2 was used, defining a lateral spatial resolution to about the same size [16].

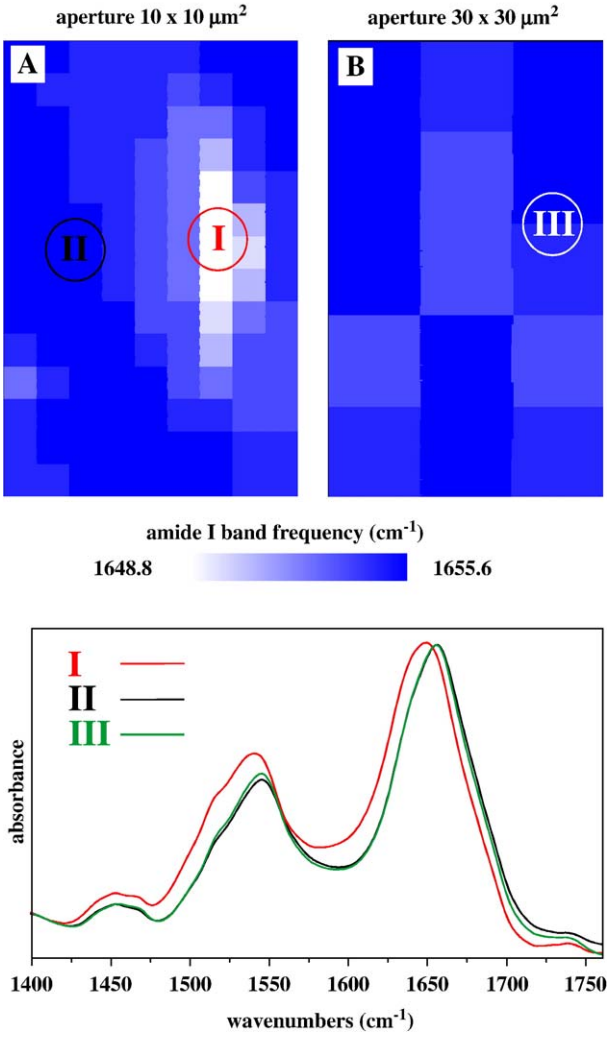

Fig. 5. Illustration of the spectral "dilution" effect of scrapie associated IR spectral features (i.e. of increased β-sheet content due to PrP^{Sc}). Panel A: frequency map reassembled from synchrotron absorbance spectra of a scrapie affected nerve cell. Aperture size: 10×10 µm^2. White regions indicate low frequency values of the amide I band and are attributed to the presence of PrP^{Sc}. Panel B: frequency map reassembled on the basis of averaged absorbance spectra simulating a virtual aperture of 30×30 µm^2 in size. Panel C, trace I: original absorbance spectrum showing scrapie associated (PrP^{sc}) features in the amide I and II region. trace II: absorbance spectrum exhibiting no signs for the presence of PrP^{sc}. trace III: spatially averaged spectrum (aperture: 30×30 µm^2) of a region known to contain PrP^{sc}. (*Spectral data provided by Dr. Janina Kneipp, Federal Institute for Materials Research and Testing).

It turned out that about one third of the nerve cells exhibited scrapie associated spectral changes. On the other hand most of the neurons displayed signs of PrP^{Sc} deposition when specifically stained by immunohistochemical techniques. The authors explained this discrepancy on the basis of detection limits and spatial resolution. First, the global concentration of PrP^{Sc} in nervous tissue barely exceeds 0.1% of the total protein content [21]. It was found in earlier studies that this is below the detection limits for PrP^{Sc} in a macroscopic FT-IR spectroscopic setup [22,23]. On the other hand, PrP^{Sc} of the scrapie strain 263K is known to form microdisperse accumulations of about 1–2 µm in diameter. Although single PrP^{Sc} accumulations of this size cannot be resolved, even by synchrotron IR microspectroscopy, tissue regions with spectroscopically detectable amounts of PrP^{Sc} were reported. As it is illustrated in Fig. 5 some of the neurons from dorsal root ganglia displayed the characteristic IR spectroscopic features of PrP^{Sc}. These features are found predominantly in the amide I/II band region and are typical for proteins rich in β-sheet structures [19].

With regard to these experimental findings it was suggested that further increase in spatial resolution would result in better detection limits for PrP^{Sc} and vice versa. The authors could show that spectral signs of PrP^{Sc} are optically "diluted" when the size of the aperture is computationally increased by averaging the spectra in the spatial domains. This situation is illustrated by Fig. 5C which compares experimental IR spectra from spots with high and low content of PrP^{Sc} (traces I and II) and an average spectrum of a virtual aperture of 30×30 µm^2 obtained from a region with high PrP^{Sc} concentration (trace III). This spectrum and the experimental spectra from regions with only low or no PrP^{Sc} content are virtually indistinguishable. Hence, the detectability of microdisperse PrP^{Sc} by IR microspectroscopy strongly depends on the size of the spatial resolution in the given microspectroscopic setup.

3.2. Spatial resolution in IR imaging of the colon mucosa

In the preceding example we have been able to use defined vibrational modes of PrP^{Sc} as infrared marker bands for scrapie. In general however, the presence of known disease marker bands is rather an exception than a rule. Typically, the disease-associated changes are found as a combination of large numbers of only subtle spectral alterations [24]. In biomedical IR spectroscopy it is therefore an accepted standard that disease recognition can be carried out best if the information content of complete spectra is systematically analyzed by multivariate data analysis methods. Hence, multivariate analysis of IR spectral patterns is fundamental to biomedical IR spectroscopy. In the following we therefore present a more typical example of how IR spectral patterns change as the spatial resolution is varied.

Table 2
Interpolation of an infrared spectral map in the spatial domains

	Map size (in pixel spectra)	Spatial resolution at 2.5 µm wavelength [in µm]
A	232×223	8.8
B	160×154	10.0[a]
C	143×137	12.0[a]
D	133×128	14.0[a]
F	80×77	18.3[b]
G	60×58	24.5[b]
H	40×38	37[b]
I	20×19	76[b]

Original map size: 1444×1388 µm^2 corresponding to 232×223 individual pixel spectra (A). The number of pixel spectra was reduced by retaining the original image aspect ratio. The spatial resolution of the original map (A) was experimentally obtained with 8.8 µm at 2.5 µm wavelength.

[a] Estimated.

[b] Pixel size.

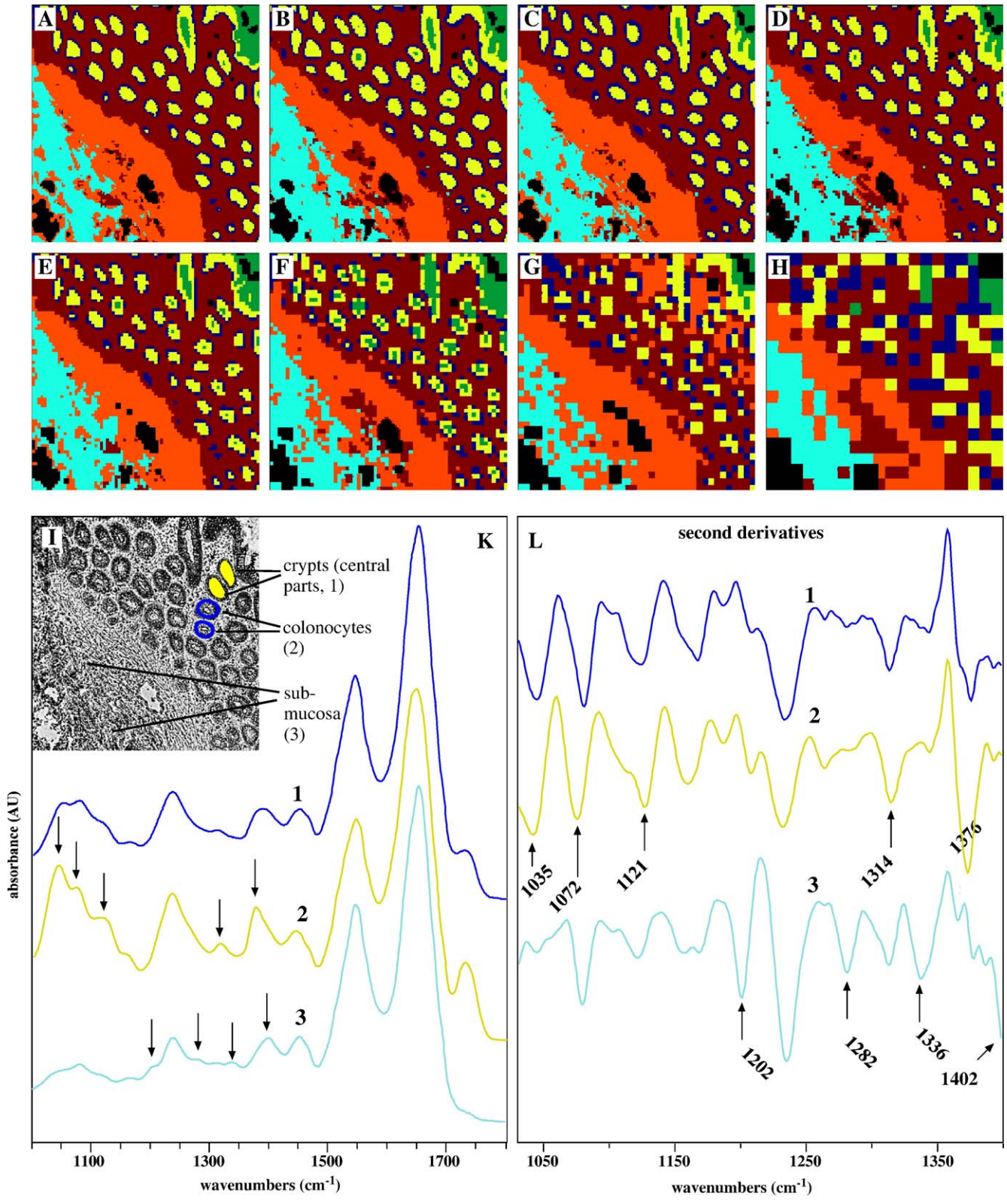

Fig. 6. IR images produced by agglomerative hierarchical clustering (AHC) and interpolation in the spatial domain from human colon mucosa sections. Panel A: AHC image (6 class classification approach) of the original IR data set (232×223 spectra. Lateral spatial resolution at 2.5 μm (4000 cm^{-1}): 8.8 μm. Panels B–H: AHC images produced after spatial interpolation (6 classes). Spatial resolution in panel B: 10 μm; C: 12 μm; D: 14 μm; E: 18.3 μm; F: 24.5 μm; G: 37 μm; H: 76 μm; Panel I: Nomarski contrast image of the unstained cryosection from the colon mucosa. Panel K: Cluster average spectra obtained from the data set of original absorbance spectra. Trace 1: class "colonocytes" (blue). Trace 2: class "central cells of the crypts" (goblet cells, yellow). Trace 3: class "submucosa" (cyan). Panel L: vector normalized second derivatives of the average spectra in panel K.

The central idea of the following example is again based on a stepwise decrease of the spatial resolution of experimental data by spectral averaging. The original infrared imaging data were recorded on a tissue section obtained by cyrosectioning a frozen tissue sample from the human colon mucosa (details of the sample preparation procedure can be found elsewhere [24]). Transmission type spectra were recorded in the 4:1 imaging mode by the PerkinElmer Spectrum Spotlight 300 IR imaging system (see Section 2.3 for experimental details).

The experimental FT-IR data comprised 232×223 (51736) microspectra. According to Table 1, the spatial resolution of the Spectrum Spotlight system in the 4:1 imaging mode is ca. 8.8 μm (Rayleigh criterion, $\lambda = 2.5$ μm). Spectral averaging was carried out by using dedicated interpolation routines of the CytoSpec software package which can be used to interpolate the data in the spectral as well as in the spatial domains [25]. In order to reduce the number of pixel spectra we have utilized spatial 2D-interpolation. An overview of the precise dimensions of the shrunken maps is given in Table 2.

Data processing included a spectral quality test, spectral preprocessing and hierarchical clustering (see ref. [26] for details). Clustering required the removal of outliers typically due to an insufficient spectral SNR. Based on the spectra which have passed the quality test, and hierarchical clustering, we produced then infrared spectral maps for the original as well as for the maps with computationally decreased spatial resolution (see Fig. 6). All cluster maps have been generated on the basis of six spectral classes. Furthermore, we have produced mean spectra for each individual cluster. Panels A–H of Fig. 6 display the series of cluster images starting with panel A for the original data (spatial resolution of 8.8 μm at 4000 cm^{-1}) and ending up with panel H for the lowest resolution (76 μm).

The spatial resolution in the examples of Fig. 6A–H was estimated on the basis of the following considerations. First, the spatial resolution in the original spectral data (6A) was obtained experimentally from the MTF (see Table 1). Second, in the highly interpolated images (6E–H) the spatial resolution is obviously not diffraction limited. As a consequence, the pixel size seems to be a good estimator to assess spatial resolution in these images. An intermediate situation is found for the images given in 6B–D.

A comparison of the Nomarski contrast image (panel I) of the unstained tissue specimen and the false color cluster maps 6A–H revealed a high degree of correspondence. As one would expect, the best correlation between histology and IR microspectroscopy can be observed at the highest spatial resolution. Interestingly, the main morphological structures of the specimen from the colon mucosa remain detectable until a particular spatial resolution threshold of about 14 μm (cf. panel 6D and Table 1). As it can be taken from panels 6E–H the class of "colonocytes", indicated by a blue circular shape in Fig. 6I, cannot be adequately resolved by IR cluster imaging above this threshold. The comparative analysis of the mean cluster spectra for colonocytes supports this finding. Fig. 7, which depicts mean absorbance spectra (left panel) and also details in the fingerprint region of these "colonocytes" mean spectra (right panel), indicates virtually no spectral changes between traces A–D (corresponding spatial resolution of 8.8–14 μm). At lateral

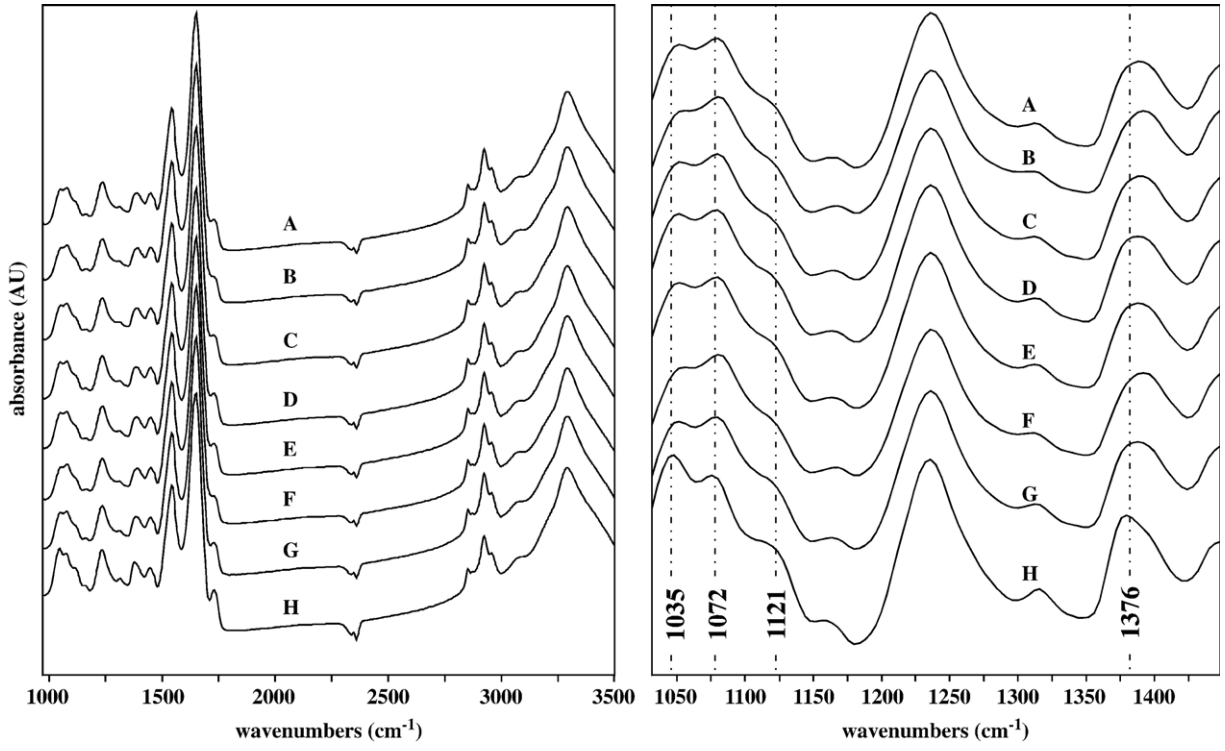

Fig. 7. Spectral changes of average spectra of the cluster "colonocytes" as a function of spatial resolution. Average spectra were obtained by agglomerative hierarchical clustering. The uppermost spectra were derived from the original absorbance spectra (spatial resolution at 4000 cm^{-1}: 8.8 μm). Decrease of spatial resolution was achieved by interpolation in the spatial domain (cf. inset, see also Table 1, Fig. 6, and text for details).

resolutions below this limit, the spectral pattern of the class colonocytes become more and more "contaminated" by spectral features arising from adjacent histological structures. In the example given in Figs. 6 and 7 these spectral "contaminations" can be attributed to IR bands of mucin, a mixture of muco- and glycoproteins. Mucin and its precursors can be found in goblet cells that represent the major cell fraction in the center of the crypts (cf. yellow elements of Fig. 6I). High concentrations of mucin are also found within the central lumen of the crypts. Mucin containing structures can be easily identified by IR spectroscopy due to the fact that mucin exhibits a series of characteristic absorbance bands in the fingerprint region of the IR spectra (1035, 1072, 1121 and 1376 cm^{-1} [27,28]. The series of cluster mean spectra for the class "colonocytes" of Fig. 7 clearly shows that spectral signs of mucin become more and more prominent as the spatial resolution is decreased. At a resolution of 76 μm (Fig. 6H and trace H of Fig. 7) even the assignment of clusters to some of the histological structures becomes questionable.

While a relatively high spatial resolution is required for resolving the colonocytes, the detection of more solid tissue structures is less dependent on this condition. We have noted for example, that spectral changes in mean cluster spectra from the submucosa do not correlate with the spatial resolution (not shown). This observation is easily understood if one takes into account that the submucosa is a morphologically more compact structure (see Figs. 6A–H showing the submucosa as cyan encoded tissue areas located in the lower left corners). Compared with the situation of colonocyte detection, spectral contaminations for the class submucosa are therefore less apparent.

From the two examples above it should be evident that a given tissue histoarchitecture determines the spatial resolution required for resolving tissue structures of interest. It has been shown for a number of examples that a moderate size of spatial resolution will be adequate. For instance, spectral signs of many solid tumors such as prostate cancer or melanoma are already detectable at a resolution of ~100 μm [29]. This is important also in the light of practicality of the IR microspectroscopic methodology. First, the spatial resolution is one of the relevant parameters with a strong impact on the spectral SNR. As many of the disease related spectral features are comparably small, a high SNR (>800) is often required in biomedical IR spectroscopy. Second, the computational requirements depend dramatically on the spatial resolution. To give an example, the amount of computer memory (RAM) required for IR image processing scales linearly with the number of pixel spectra, and is consequently – at an adequate rate of oversampling – inversely related with the spatial resolution squared. Thus, an inadequate spatial resolution may have a significant impact on image processing speed (cluster imaging) or even force a reduction of the sample area which was intended to study.

There is some hope that further improvements of the IR microspectroscopic instrumentation such as more sensitive detectors or new experimental designs [30–32], but also new computer hardware will considerable improve the capabilities of the technique. From the examples above it should be, however, clear that the spatial resolution defines the character and type of spectral patterns that are obtained.

The latter statement is crucial for research in the field IR imaging of tissues. We wish to emphasize, that the problem of specifying spatial resolution is not only a question of images that are too coarse or too fine. As we have noted earlier, infrared spectral patterns themselves change as the lateral resolution is varied. In consequence, current spectral data bases of tissue spectra will be valid only for exactly one size of spatial resolution. This is essential since we believe that an automatic routine for objective classification of tissue microspectra will be based on supervised classification models that are trained and validated with carefully selected reference spectra [11,24,29]. Thus, the definition of a particular spatial resolution is a key parameter for the acquisition of spectra for tissue data bases.

One natural way of addressing this particular problem would be a computational procedure that could be used to synchronize the resolution of the spectra to be classified and the specifications of the classifier. Such a routine could be added to the standard preprocessing procedures such as quality tests, derivation, or normalization, but would be functioning only to reduce the resolution.

4. Increasing spatial resolution by 3D-Fourier self-deconvolution (FSD)

In the previous chapters we have pointed out a number of theoretical and experimental factors which restrict the spatial resolution in IR microspectroscopy. In the following we introduce an alternative computational approach for increasing the lateral spatial resolution. Aside from a short and simplified theoretical description of the basic principles of 3D-Fourier self-deconvolution we will give also an experimental example that illustrates how this technique may work in practice.

Deconvolution of experimental data is carried out since many years in various research areas. For example, this technique is routinely applied in the field of microscopic imaging to increase the image contrast in the two lateral directions. Ideally, deconvolution of a particular image is achieved by employing the point spread function (PSF) of the optical system utilized for image acquisition. [33–35].

On the other hand, spectroscopists, and IR spectroscopists in particular, are quite familiar with the concept of Fourier self-deconvolution (FSD). This method was presented 25 years ago as a technique to computationally resolve overlapped IR bands from spectra of condensed phase samples [36–39]. The higher resolution obtained by FSD in the spectral domain have been employed in countless studies, particularly in the field of protein structure analysis [40,41].

Each of the distinct IR microspectroscopic imaging techniques delivers the spectral information in the form of the well-known spectral hypercube [42]. In this hypercube the spectral information (mostly absorbance or transmittance data) is arranged in a three-dimensional grid spanned by one spectral and two spatial axes. The hypercube is often represented as a series of chemical images, or as a *xy*-array of spatially

resolved IR spectra. Naturally, deconvolution of the IR imaging data could be carried out along the *xy*-directions (deconvolution of chemical images) but also in the hypercube's *z*-direction, i.e., in the spectral domain. Nevertheless we believe that an approach that combines both, the imaging and the spectral deconvolution approach would provide a much higher image contrast compared with the contrast that would be obtained by spectral, or image deconvolution alone. As the 3D-deconvolution procedure adapted by us follows basic principles of FSD we will continue with a short introduction into the theory of FSD.

4.1. Theory of FSD and 3D-FSD

Infrared spectroscopic data obtained from biomedical samples such as cells and tissues can be generally characterized by strongly overlapping, spectroscopically unresolvable band composites. Generally, the width of individual absorption bands in these spectra is larger than the separation between neighboring bands. Therefore, an increase of the instrumental (spectral) resolution does not result in a better band separation [36,43].

A number of mathematical methods have been proposed in the past to resolve broad band contours into their individual constituents [36,44,45]. Among these, the method of Fourier self-deconvolution (FSD) still enjoys increasing popularity. As a very short introduction into the basic principles of FSD, the method of band narrowing in FSD starts with the assumption that an experimental spectrum $E(\nu)$ can be represented by a convolution of a deconvolved spectrum $E'(\nu)$ and a line shape function $L(\nu)$, ($\circ$ indicates the convolution operation):

$$E(\nu) = E'(\nu) \circ L(\nu) \tag{5}$$

$E(\nu)$ is a spectrum with sharp lines with the intensities E at the wavenumber ν. It is known that convolution in the spectral domain corresponds to multiplication in the interferogram domain (Fourier space). After inverse Fourier transformation of Eq. (5) one yields the following relation:

$$I(s) = I'(s) \cdot \ell(s) \tag{6}$$

$I(s)$, $I'(s)$ and $\ell(s)$ are the inverse Fourier transforms of $E(\nu)$, $E'(\nu)$ and $L(\nu)$, respectively. The effect of the line shape function $L(\nu)$ can now be eliminated in Fourier space by dividing Eq. (6) by $\ell(s)$. Next, the deconvolved spectrum $E'(\nu)$ is obtained by a forward Fourier transformation:

$$E'(\nu) = FT\left\{\frac{I(s)}{\ell(s)}\right\} \tag{7}$$

In this way, convolution of the experimental spectrum by the lineshape function $L(\nu)$ can be eliminated. The procedure of Fourier self-deconvolution for IR spectra of condensed phase samples was first described by Stone [44] and was further developed by Kauppinen et al. in a series of three publications [36–38]. The authors noted in their pioneering work that the application of the deconvolution technique to experimental spectra is less trivial. First, the proper form of the line shape function $L(\nu)$ is unknown. Furthermore, noise which is always present in real spectra is strongly amplified by the FSD technique. Kauppinen and coworkers addressed these problems by suggesting a deconvolution procedure that considers a Lorentzian band function $E(\nu)$ in the spectral domain:

$$E(\nu) = \frac{\delta}{\pi \cdot [\delta^2 + (\nu - \nu_0)^2]} \xrightarrow{inv\ FT}$$

$$I(s) = e^{-2\pi\delta|s|} \cdot 2\cos(2\pi\nu_0 s) \tag{8}$$

where 2δ is the full width at half height (FWHH) and ν_0 is the wavenumber position of the Lorentzian's band maximum. To reduce the effects of noise amplification in the FSD procedure Kauppinen et al. proposed furthermore to introduce an additional damping function $D(s)$ which should by multiplied with the exponential deconvolution function in the interferogram domain:

$$\ell(s) = D(s) \cdot e^{2\pi\delta|s|} \tag{9}$$

with

$$D(s) = \left(1 - \frac{|s|}{k}\right)^2 \tag{10}$$

$D(s)$ has the effect of an apodization function and is always zero for $|s| \geq k$. It is not the objective of this work to discuss details of the Fourier self-deconvolution technique (the reader is referred to the original work [36–38]). At this point it should be noted only that a major drawback of the FSD is its subjectivity. The authors themselves explicitly stated that the output of the FSD method "depends somewhat on the practitioner" [39] as it is always required to watch for additional "side lobes", indicating that the spectrum has been "overdeconvolved".

For deconvolution of 3D-IR imaging data we have used the basic ideas of the 1D-FSD methodology. In analogy to Eq. (9) a 2-dimensional spatial convolution function $\ell(\xi,\psi)$ can be defined for the Fourier transforms of the spatial components *xy*. This function is then multiplied by Eq. (9):

$$\ell(\xi, \psi, s) = D(\xi, \psi, s) \cdot e^{2\pi(\delta_\xi|\xi| + \delta_\psi|\psi| + \delta_s|s)|)} \tag{11}$$

The parameters δ_ξ, δ_ψ, and δ_s denote the half width at half height for the "bands" in the spatial (*xy*) and the spectral (ν) dimensions. As δ in spectral 1D-FSD they can be considered as band narrowing factors.

Eq. (11) contains also the 3D-damping function $D(\xi,\psi,s)$. The function is modified such that it contains squared counterparts for the expression ($|s|/k$) of Eq. (10). The result of this modification is a more effective noise suppression:

$$D(\xi, \psi, s) = \left[1 - \left(\frac{|\xi|}{k_\xi}\right)^2\right]^2 \cdot \left[1 - \left(\frac{|\psi|}{k_\psi}\right)^2\right]^2 \cdot \left[1 - \left(\frac{|s|}{k_s}\right)^2\right]^2 \tag{12}$$

The k-parameters can be referred to as a factors reducing noise amplification by the 3D-FSD procedure. Note that the function $D(\xi,\psi,s)$ is always zero for $k_\xi \geq |\xi|$; $k_\psi \geq |\psi|$ and $k_s \geq |s|$. In the practical software implementation [25] we have normalized k_i by ξ_{max}, ψ_{max}, or s_{max}, respectively with $0 \leq k_i \leq 1$.

4.2. Practical limitations of 3D-FSD

The choice of useful parameters for Fourier self-deconvolution is subjective and the results of 3D-FSD strongly depend on the experience of the experimentator [36,46]. Furthermore, aside from this human factor in post-collection data processing, possible sources of error are often inappropriate measurement conditions.

First of all, deconvolution requires a sufficiently high spectral signal to noise ratio (SNR). In FT-IR imaging many experimental parameters such as the aperture size, data collection time (number of scans), or sample thickness, to mention only a few, influence the SNR. As it is not the objective of this work to discuss the details of achieving optimal SNR the reader is referred to the exhaustive work of Griffiths, de Haseth and Wetzel describing general and practical aspects of the SNR in FT-IR spectroscopy [47] and microspectroscopy [5].

A second important issue directly related to the applicability of 3D-FSD to IR imaging data sets is the need for oversampling. According to Shannon's sampling theorem [17] the sampling interval must be at least twice the signal bandwidth. For signals such as IR spectra of the condensed phase the width of the individual infrared absorption bands is in most cases much higher than the common standard of the instrumental (physical) resolution of 4 or 2 cm^{-1}. This precondition should be also met in the spatial domains: the aperture size should be larger by a factor of 2 (or more) than the step size of motorized microscope stage in x and y directions. Furthermore, the topology of the samples should ideally not contain structures with a higher spatial frequency i.e. the signal must be bandlimited. Obviously, the need for oversampling as a precondition for 3D-FSD applies also to FT-IR microspectroscopic imaging systems with fixed detector geometry (FPA).

A third important source of error in 3D-FSD of IR microspectroscopic data arises from uncompensated contributions from atmospheric water vapor. Typical spectral features of water vapor are generally bands which are significantly sharper than any sample specific band. Water vapor bands are consequently intensified by FSD to such a degree that spectral information of the sample may be strongly overlaid [46]. Similar effects of spectral distortions can principally also occur in sample

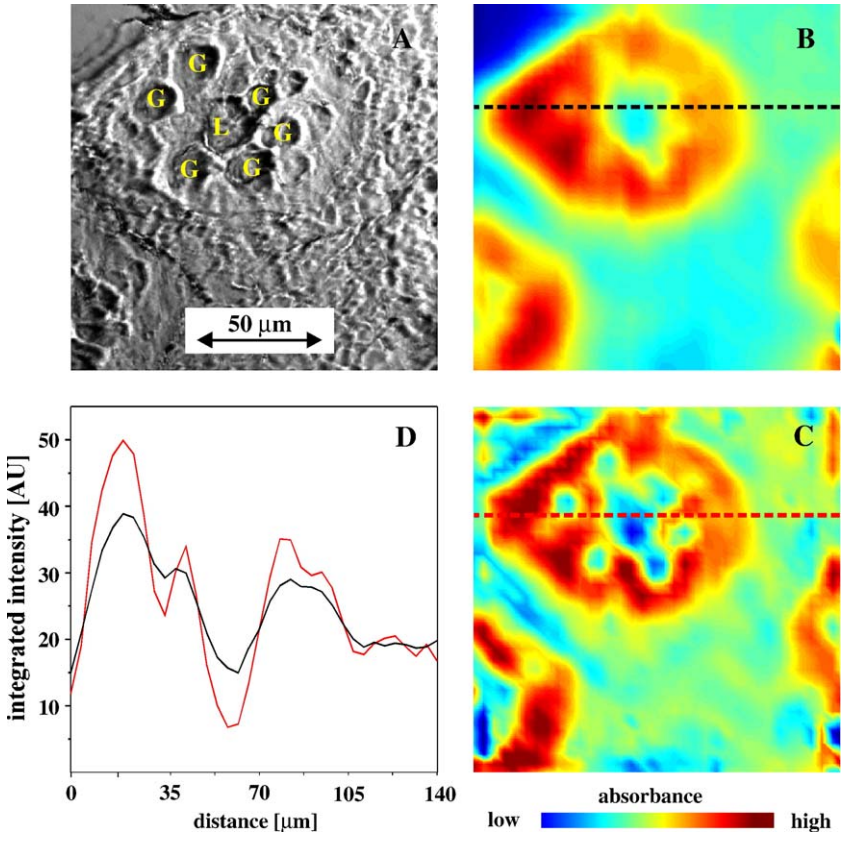

Fig. 8. Example of resolution enhancement by 3D-Fourier self-deconvolution. Panel A: Nomarski contrast image of a thin section from the colon mucosa. The upper-central area displays a cross sectioned crypt with a central lumen (L) and individual goblet cells (G). Panel B: chemical image assembled on the basis of baseline-corrected absorbance spectra using the integrated absorbance of the amide I band (1620–1680 cm^{-1}). Panel C: chemical image assembled after applying 3D-Fourier self-deconvolution (FSD). Imaging parameter: baseline correction, area of the amide I band (1620–1680 cm^{-1}). Panel D: Comparison of intensity profiles obtained from original data (black curve) and 3D-FSD data (red curve).

regions with contributions from substances of non-biological origins such as tissue embedding medium. Thus, eliminating spectral contributions arising from water vapor, embedding medium or a supportive substrate such as polyethylene films is an essential prerequisite for 3D-FSD.

The fourth problem of 3D-FSD that must be addressed at this point is related to the wavelength dependence of the spatial resolution. From Eq. (1) it is obvious that the spatial resolution at diffraction limited conditions is much higher for shorter than for longer wavelengths. This implies that a deconvolution procedure in the spatial domains should somehow consider this wavelength dependence. It would be principally conceivable to introduce additional wavelength-dependent functions for the spatial band narrowing $\delta_\xi(\lambda)$, $\delta_\psi(\lambda)$ and the noise damping factors $k_\xi(\lambda)$, $k_\psi(\lambda)$. However, such a wavelength correction routine is currently not available in our software implementation of 3D-FSD. We therefore recommend to apply the 3D-deconvolution algorithm presented in Section 4.1 to relatively narrow regions of the infrared spectrum (e.g. from 1000 to 1600 cm^{-1}), only.

The latter statements of the wavelength dependence of the spatial resolution are not only relevant to 3D-FSD. The fact, that at diffraction limited conditions (synchrotron, small apertures) the spatial resolution in the CH-stretching region (2800–3100 cm^{-1}) is more than three time higher compared with the resolution for the $\nu_{sy}PO_2^-$ modes at (1088 cm^{-1}) has been only rarely discussed in the literature of biomedical IR microspectroscopy. Thus, such a wavelength correction routine would be required not only as a part of 3D-FSD, but should be generally precluded to standard spectral preprocessing routines of IR imaging. However, to remove subjectivity of 3D-FSD, which lies in the definitions of the δ and k-factors, the precise expression of the wavelength-dependent point spread function (PSF) for the most relevant IR imaging device would be required. These PSF could be used in a better, i.e. an analytical way for deconvolution of diffraction limited IR imaging data sets. However, as long as these instrument-specific PSFs are not available, our proposed empiric approach might be useful to increase the parameter of lateral spatial resolution in IR microspectroscopic imaging.

4.3. Example of resolution enhancement by 3D-Fourier self-deconvolution

Fig. 8 displays an example of resolution enhancement by 3D-Fourier self-deconvolution. In panel A of Fig. 8 a Nomarski contrast image of a cross-sectioned individual crypt from the colon mucosa is shown. Colonic crypts are several hundred microns deep, tube-like epithelial invaginations with a diameter of about 50–100 μm. Mucin producing goblet cells (G) are clustered around a central lumen (L) of these tubular glands.

The tissue region shown in Fig. 8A was investigated by synchrotron FT-IR microspectroscopic imaging at the U10B beamline of the National Synchrotron Light Source (NSLS) in Brookhaven. The microspectrometer at this beam line is a Nicolet Magna 860 FT-IR spectrometer coupled to a Spectra Tech Continuum IR microscope and controlled by Nicolet's data acquisition program Omnic E.S.P. and the Atlμs mapping software package (Nicolet Madison, WI). The microscope was equipped with a computer-controlled xy-stage. Due to the highly collimated IR-beam of the synchrotron source, an aperture as small as 8×8 μm^2 could be used with adequate signal to noise quality.

Altogether, 1296 high-resolution FT-IR spectra (36×36) from a tissue area of 140×140 μm^2 were collected in transmission mode. Spatial oversampling was achieved by specifying a microscope stage step size of 4 μm in x and y direction, respectively. Nominal spectral resolution was 8 cm^{-1} and a Happ–Genzel function was used for apodization. Interferograms of 64 single scans were co-added per single spectrum.

The procedure of sample preparation included cryosectioning and thaw mounting onto CaF_2-windows with a thickness of 1 mm.

For 3D-FSD we have used values of 0.3 for k_ξ and k_ψ respectively, and 0.5 for k_s. For δ_ξ, δ_ψ, and δ_s a value of 15 was applied.

Panel B of Fig. 8 shows a chemical image produced from baseline corrected original absorbance spectra. This map was reassembled on the basis of integrated absorbance values of the amide I band (1620–1680 cm^{-1}). Fig. 8B clearly demonstrates that main morphologic structures such as the crypts in total, or the crypt's central lumen can be visually identified. On the other hand, individual goblet cells denoted by the letter "G" in Fig. 8A are not resolved in this image. A higher image contrast could be achieved after 3D-FSD (see map C of Fig. 8). Map C was again reassembled by color scaling baseline corrected integrated intensities between 1620–1680 cm^{-1}. Individual goblet cells are resolved and can be now identified unambiguously.

A line scan through the crypt in the upper central area (see dotted lines in 8B/C) is given in panel D of Fig. 8. These intensity profiles were derived from the original absorbance spectra (black curve) and the FSD data (red curve) and demonstrate the increased image contrast in the FSD map. As the concept of spatial resolution is inseparable from the contrast, the example of Fig. 8 unequivocally shows that the procedure of 3D-FSD is principally suitable to increase the spatial resolution in IR microspectroscopic imaging.

5. Conclusions

Spatial resolution is one of the most critical measurement parameters in infrared microspectroscopy. Due to the distinct levels of morphologic heterogeneity in cells and tissues the spatial resolution in a given IR imaging setup strongly affects the character of the infrared spectral pattern obtained from the biomedical samples. This is particularly important when spectral data bases of reference microspectra from defined tissue structures are collected.

In this paper we have also pointed out that the concept of spatially resolution in IR imaging is inseparable from the contrast. Based on infrared microspectroscopic transmittance data acquired from an USAF 1951 resolution target we have demonstrated how the spatial resolution can be determined

experimentally and some numbers for the spatial resolution of popular IR imaging systems are provided.

Finally, we have presented a new computational procedure which is suitable to improve the spatial resolution in IR imaging. A theoretical model of 3D-Fourier self-deconvolution (FSD) is given and advantages or pitfalls of this method are discussed. Based on synchrotron IR microspectroscopic data we have furthermore demonstrated that the technique of 3D-FSD can be successfully applied to increase the spatial resolution in a real IR imaging setup.

Acknowledgements

We thank Prof. Max Diem (Northeastern University, Boston) and Dr. Janina Kneipp (Federal Institute for Materials Research and Testing-BAM) for fruitful discussions, support and providing experimental data, Dr. Ulrich Schade (IRIS@BESSY, Berlin-Adlershof) for carefully reading of the manuscript, Dr. Richard A. Spragg (PerkinElmer Life and Analytical Sciences) for help and assistance during the measurements at the PerkinElmer application labs, and Dr. Lisa Miller and Dr. Lawrence Carr (U10B@NSLS, Upton) for their help and fruitful discussions at the Brookhaven National Laboratory. Furthermore we are grateful to Dr. Milos D. Miljkowicz (Northeastern University, Boston), Dr. Matthias Boese (Bruker Optik GmbH) and Dr. David Moss (IR 1/2 @ANKA, Karlsruhe) for conducting the USAF 1951 resolution target measurements. We also acknowledge tissue sources from the Robert-Rössle-Klinik at the Max-Delbrück-Centrum (MDC) in Berlin-Buch and thank Dr. Wolfgang Haensch for providing his histological expertise.

References

[1] M.A. Harthcock, S.C. Atkin, Imaging with functional group maps using infrared microspectroscopy, Appl. Spectrosc. 42 (3) (1988) 449–455.
[2] N. Jamin, P. Dumas, J. Moncuit, W.H. Fridman, J.L. Teillaud, G.L. Carr, G.P. Williams, Highly resolved chemical imaging of living cells by using synchrotron infrared microspectrometry, Proc. Natl. Acad. Sci. U. S. A. 95 (9) (1998) 4837–4840.
[3] L.H. Kidder, I.W. Levin, E.N. Lewis, V.D. Kleiman, E.J. Heilweil, Mercury cadmium telluride focal-plane array detection for mid-infrared Fourier-transform spectroscopic imaging, Opt. Lett. 22 (10) (1997) 742–744.
[4] B.R. Wood, L. Chiriboga, H. Yee, M.A. Quinn, D. McNaughton, M. Diem, Fourier transform infrared (FTIR) spectral mapping of the cervical transformation zone, and dysplastic squamous epithelium, Gynecol. Oncol. 93 (1) (2004) 59–68.
[5] D.L. Wetzel, S.M. LeVine, Biological Applications of Infrared Spectroscopy, in: H.U. Gremlich, B. Yan (Eds.), Infrared and Raman Spectroscopy of Biological Materials, Marcel Dekker Inc, New York, 2000.
[6] E.N. Lewis, A.M. Gorbach, C. Marcott, I.W. Levin, High-fidelity Fourier transform infrared spectroscopic imaging of primate brain tissue, Appl. Spectrosc. 50 (2) (1996) 263–269.
[7] L.H. Kidder, V.F. Kalasinsky, J.L. Luke, I.W. Levin, E.N. Lewis, Visualization of silicone gel in human breast tissue using new infrared imaging spectroscopy, Nat. Med. 3 (2) (1997) 235–237.
[8] P. Lasch, L. Chiriboga, H. Yee, M. Diem, Infrared spectroscopy of human cells and tissue: detection of disease, Technol. Cancer Res. Treat. 1 (1) (2002) 1–7.
[9] L.P. Choo, D.L. Wetzel, W.C. Halliday, M. Jackson, S.M. LeVine, H.H. Mantsch, In situ characterization of β-amyloid in Alzheimer's diseased tissue by synchrotron FTIR microspectroscopy, Biophys. J. 71 (1996) 1672–1679.
[10] B.R. Wood, K.R. Bambery, L.M. Miller, M. Quinn, L. Chiriboga, M. Diem, D. McNaughton, Infrared imaging of normal and diseased cervical tissue sections, Proc.-SPIE 5651 (2005) 78–84.
[11] P. Lasch, W. Waesche, U. Bindig, D. Naumann, G.J. Mueller, FT-IR microspectroscopic imaging of human carcinoma thin tissue sections, Proc.-SPIE 3197 (1997) 278–285.
[12] E.H.K. Stelzer, Contrast, resolution, pixelation, dynamic range and signal-to-noise ratio: fundamental limits to resolution in fluorescence light microscopy, J. Microsc. 189 (1) (1997) 15–24.
[13] T. Lehman, W. Oberschelp, E. Pelikan, R. Repges, Bildverarbeitung für die Medizin, Springer Verlag, Berlin Heidelberg, New York, 1997.
[14] K. Nishikida, Spatial resolution in infrared microscopy and imaging. thermo electron corporation, Application Note 50717 (2005).
[15] J.A. Reffner, Instrumental factors in infrared microspectroscopy, Cell. Mol. Biol. (Noisy-le-Grand) 44 (1) (1998) 1–7.
[16] G.L. Carr, Resolution limits for infrared microspectroscopy explored with synchrotron radiation, Rev. Sci. Instrum. 72 (3) (2001) 1613–1619.
[17] C.E. Shannon, Communications in the presence of noise, Proc. IRE 37 (1949) 10–21.
[18] H. Nyquist, Certain topics in telegraph transmission theory, AIEE Trans. 47 (1928) 617–644.
[19] J. Kneipp, L.M. Miller, M. Joncic, M. Kittel, P. Lasch, M. Beekes, D. Naumann, In situ identification of protein structural changes in prion-infected tissue, Biochim. Biophys. Acta 1639 (3) (2003) 152–158.
[20] J. Kneipp, L.M. Miller, S. Spassov, F. Sokolowski, P. Lasch, M. Beekes, D. Naumann, Scrapie-infected cells, isolated prions, and recombinant prion proteins: a comparative study, Biopolymers (Biospectroscopy) 74 (1,2) (2004) 163–167.
[21] M. Beekes, E. Baldauf, S. CaMens, H. Diringer, P. Keyes, A.C. Scott, G.A. H. Wells, P. Brown, C.J. Gibbs Jr., D.C. Gajdusek, Western blot mapping of disease-specific amyloid in various animal species and humans with TSEs using a high-yield purification method, J. Gen. Virol. 76 (1995) 2567–2576.
[22] J. Kneipp, P. Lasch, E. Baldauf, M. Beekes, D. Naumann, Detection of pathological molecular alterations in scrapie-infected hamster brain by Fourier transform infrared (FT-IR) spectroscopy, Biochim. Biophys. Acta 1501 (2000) 189–199.
[23] J. Kneipp, M. Beekes, P. Lasch, D. Naumann, Molecular changes of preclinical scrapie can be detected by infrared spectroscopy, J. Neurosci. 22 (8) (2002) 2989–2997.
[24] P. Lasch, W. Haensch, L. Kidder, E.N. Lewis, D. Naumann, Colorectal adenocarcinoma characterization by spatially resolved FT-IR microspectroscopy, Appl. Spectrosc. 56 (1) (2002) 1–9.
[25] CytoSpec Website. http://www.cytospec.com [01. December 2005].
[26] P. Lasch, W. Haensch, D. Naumann, M. Diem, Cluster analysis of colorectal adenocarcinoma imaging data: A FT-IR microspectroscopic study, Biochim. Biophys. Acta—Molecular Basis of Disease 1688 (2) (2004) 176–186.
[27] M. Jackson, H.H. Mantsch, FT-IR spectroscopy in the clinical science. Biomedical Applications of Spectroscopy, John Wiley and Sons Ltd, 1996.
[28] L. Chiriboga, P. Xie, W. Zhang, M. Diem, Infrared spectroscopy of human tissue: III. Spectral differences between squamous and columnar tissue and cells from the human cervix, Biospectroscopy 3 (1997) 253–257.
[29] P. Lasch, D. Naumann, FT-IR microspectroscopic imaging of human carcinoma thin sections based on pattern recognition techniques, Cell. Mol. Biol. (Noisy-le-Grand) 44 (1) (1998) 189–202.
[30] F. Keilmann, Vibrational-infrared near-field microscopy, Vib. Spec. 29 (1–2) (2002) 109–114.
[31] B. Knoll, F. Keilmann, Mid-infrared scanning near-field optical microscope resolves 30 nm, J. Microsc. 194 (1999) 512–515.
[32] A. Dazzi, R. Prazeres, F. Glotin, J.M. Ortega, Local infrared microspectroscopy with subwavelength spatial resolution with an atomic force microscope tip used as a photothermal sensor, Opt. Lett. 30 (18) (2005) 2388–2390.
[33] J. Boutet de Monvel, S. Le Calvez, M. Ulfendahl, Image restoration for confocal microscopy: improving the limits of deconvolution, with

application to the visualization of the mammalian hearing organ, Biophys. J. 80 (2001) 2455–2470.
[34] J.B. Sibarita, Deconvolution microscopy, Adv. Biochem. Eng. Biotechnol. 95 (2005) 201–243.
[35] M. Von Tiedemann, A. Fridberger, M. Ulfendahl, J.B. De Monvel, Image adaptive point-spread function estimation and deconvolution for in vivo confocal microscopy, Microsc. Res. Tech. 69 (1) (2006) 10–20.
[36] J.K. Kauppinen, D.J. Moffat, H.H. Mantsch, D.G. Cameron, Fourier self-deconvolution: a method for resolving intrinsically overlapped bands, Appl. Spectrosc. 35 (3) (1981) 271–276.
[37] J.K. Kauppinen, D.J. Moffat, H.H. Mantsch, D.G. Cameron, Self-deconvolution and first order derivatives using Fourier transforms, Anal. Chem. 53 (9) (1981) 1454–1457.
[38] J.K. Kauppinen, D.J. Moffat, H.H. Mantsch, D.G. Cameron, Noise in Fourier self-deconvolution, Appl. Optics. 20 (3) (1981) 1866.
[39] D.J. Moffat, J.K. Kauppinen, H.H. Mantsch, Computers and infrared spectroscopy: evolution and revolution, Can. J. Chem. 69 (1991) 1781–1785.
[40] W.J. Yang, P.R. Griffiths, M. Byler, H. Susi, Protein conformation by infrared spectroscopy: resolution enhancement by Fourier self-deconvolution, Appl. Spectrosc. 39 (2) (1985) 228–281.
[41] W.K. Surewicz, H.H. Mantsch, D. Chapman, Determination of protein secondary structure by Fourier transform infrared spectroscopy: a critical assessment, Biochemistry 32 (1993) 389–394.
[42] M.D. Schaeberle, I.E. Levin, E.N. Lewis, Biological vibrational spectroscopic imaging, in: H.U. Gremlich, B. Yan (Eds.), Infrared and Raman Spectroscopy of Biological Materials, Marcel Dekker Inc, New York, 2000.
[43] W. Herres, J. Gronholz, Understanding FT-IR data processing, Reprint Vols. 1(84), 3(85) Dr. Alfred Huethig Publishers (obtainable from Bruker Optik, Karlsruhe).
[44] H. Stone, Mathematical resolution of overlapping bands, J. Opt. Soc. Am. 52 (1962) 998–1003.
[45] F. Holler, D.H. Burns, J.B. Callis, Direct use of second derivatives in curve-fitting procedures, Appl. Spectrosc. 43 (5) (1989) 877–882.
[46] H.H. Mantsch, D.J. Moffatt, H. Casal, Fourier transform methods for spectral resolution enhancement, J. Mol. Struct. 173 (1988) 285–298.
[47] P.R. Griffiths, J.A. de Haseth, Signal-to-Noise ratio, Fourier Transform Infrared Spectroscopy, John Wiley and Sons, New York, 1986.